ADVANCED OPTICAL MATERIALS
www.advopticalmat.de

# Large-Scale Laser Nanopatterning of Multiband Tunable Mid-Infrared Metasurface Absorber

*Dandan Yuan, Jun Li, Jiaxu Huang, Min Wang, Shaolin Xu,* and Xinwei Wang*

**Large-scale nanopatterning at low cost and high throughput is crucial to the practical applications of metasurfaces. Phase-change materials equipped in these metasurfaces as modulation layers or resonators are generally applied to achieve a tunable function and have attracted significant attention. Here, an efficient method is developed by combining ultrafast laser localized modification/ablation and subsequent etching to fabricate nanostructures on a phase-change material, $Ge_2Sb_2Te_5$ (GST), over a wafer-sized area. The localized laser treatments under gradually increased laser fluences contribute to the variety of achievable nanostructures including disk and ring structures, whose feature sizes and periods can be tuned by adjusting laser parameters and subsequent etching conditions. A mid-infrared metasurface absorber is designed and fabricated by using the GST ring units as resonators. Notably, varying the geometrical features of rings allows generating dual-band and tri-band absorption peaks in the mid-infrared spectral range, whose peak absorptivity can reach ≈92%. By converting GST from amorphous to crystalline state, a broad absorption spectral redshift of 700 nm is achieved. The large-area high-throughput fabrication together with high-absorption design demonstrates their potential in mass production of phase-change metasurface-based absorbers.**

## 1. Introduction

Metasurface is a planar form of metamaterial that consists of a series of elaborately designed sub-wavelength structures.[1] As one of the achievable functions of metasurfaces, high light absorption has attracted considerable attention for its promising applications in areas such as thermal emission,[2] sensing,[3,4] and spectroscopy.[5] To achieve high absorption, the majority of metasurface-based absorbers are designed with a metallic ground layer and an upper metallic resonator array separated by a dielectric spacer.[6–8] The metallic ground layer is employed not only to block the transmission channel but also to interact with the upper metallic resonators to generate strong electric and magnetic resonances.

For most metasurface absorbers, the working bands are fixed after design and fabrication, which are unsuitable for scenes requiring tunable frequencies.[9,10] To meet the tunable requirements, phase-change materials, like $Ge_2Sb_2Te_5$ (GST), are widely applied as a modulation medium in the design of metasurfaces. GST can be switched between amorphous and crystalline phases with different optical properties under appropriate optical,[11] electrical,[12,13] or external-heating[14] stimuli. Optically triggered phase transition can occur in nanoseconds time scale and support a large number of rewriting cycles.[15,16] Once the phase change is accomplished, GST can maintain its phase state for years at room temperature. With these excellent properties, GST has drawn researchers' interest in achieving tunable or switchable metasurfaces.[17–20] When GST is applied in the metasurface-based absorbers, the typical way is to use the GST layer as a modulation layer sandwiched between a metallic ground layer and upper patterned metallic resonators.[21–23] Another way is that GST microstructures are directly employed as resonators, such as some thermal emitters characterized by absorption.[24,25] For the former, the structural size of the upper metallic resonators is usually required to be subwavelength, nanofabrication methods including electron beam lithography (EBL) and focused ion beam (FIB) are commonly used. These methods generally suffer from high-cost, low-throughput, and small processing area, which restricts practical applications of metasurface-based absorbers. Efforts were also made by researchers to achieve large-area phase-change absorbers, such as using an anodic aluminum oxide (AAO) nanomask for depositing Al nanoparticles,[26] whereas the flexibility of this kind of method is generally limited. For the studies of thermal emitters that directly utilize GST microstructures as resonators, the fabrication of the

D. Yuan
School of Mechatronics Engineering
Harbin Institute of Technology
Harbin 150001, P. R. China

D. Yuan, J. Li, J. Huang, S. Xu
Department of Mechanical and Energy Engineering
Southern University of Science and Technology
Shenzhen 518055, P. R. China
E-mail: xusl@sustech.edu.cn

M. Wang
School of Microelectronics
Southern University of Science and Technology
Shenzhen 518055, P. R. China

X. Wang
Department of Mechanical Engineering
Iowa State University
Ames, IA 50011, USA

The ORCID identification number(s) for the author(s) of this article can be found under https://doi.org/10.1002/adom.202200939.

**DOI: 10.1002/adom.202200939**

 

GST resonators is usually performed by a relatively complicated photolithographic method.

Ultrafast laser ablation has been widely used as a low-cost and flexible method for achieving large-area nanostructured surface,[27] which can also be used for locally inducing the phase change of GST.[28] It is interesting to find that the amorphous and laser-induced crystallized phases of GST demonstrate different etching rates under specific etchants, which makes the micro/nanostructures on GST achievable by combining localized laser-induced phase change and subsequent wet etching process.[29–33] This mask-free laser surface structuring technique is potential for large-area nanopatterning of phase-change metasurface at low cost. More systematic processing optimization and thorough designs need to be done to bring this fabrication technique into realization of a useful large-area functional device.

In this work, we report the design, fabrication, and characterization of large-area, multiband and tunable phase-change metasurface absorbers by exploiting the method of combining laser localized ablation and subsequent etching. Nanostructured GST film is introduced to act as resonators, and a gold ground layer is utilized to block the transmission channel, thus this kind of structure can achieve high absorption. The relationship between the laser fluence and the morphology of achievable structures has been thoroughly studied. Disk and ring structures of GST with varied feature sizes and periods are fabricated by tuning separate Gaussian-distributed pulse laser irradiation and subsequent etching conditions. It is noted that the ring structures that are generally difficult to make can be easily fabricated with tunable feature sizes by this method. As a demonstration, we utilize crystallized GST rings as the resonant units in a large area ($3 \times 3$ cm$^2$) and successfully achieve tunable multiband meta-absorbers in the mid-infrared spectrum. The varied sizes of rings empower the ring-based absorbers to achieve both dual-band and tri-band mid-infrared absorption. Additionally, by exploiting the amorphous-to-crystalline phase transition of the GST modulation layer, the absorption peaks of the GST-based absorber can achieve a pronounced redshift up to 700 nm.

## 2. Results and Discussion

### 2.1. Construction and Fabrication of the Absorber

The metasurface absorber is designed with crystalline GST resonator arrays embedded inside an amorphous GST film as shown in **Figure 1**a by considering the characteristics of the

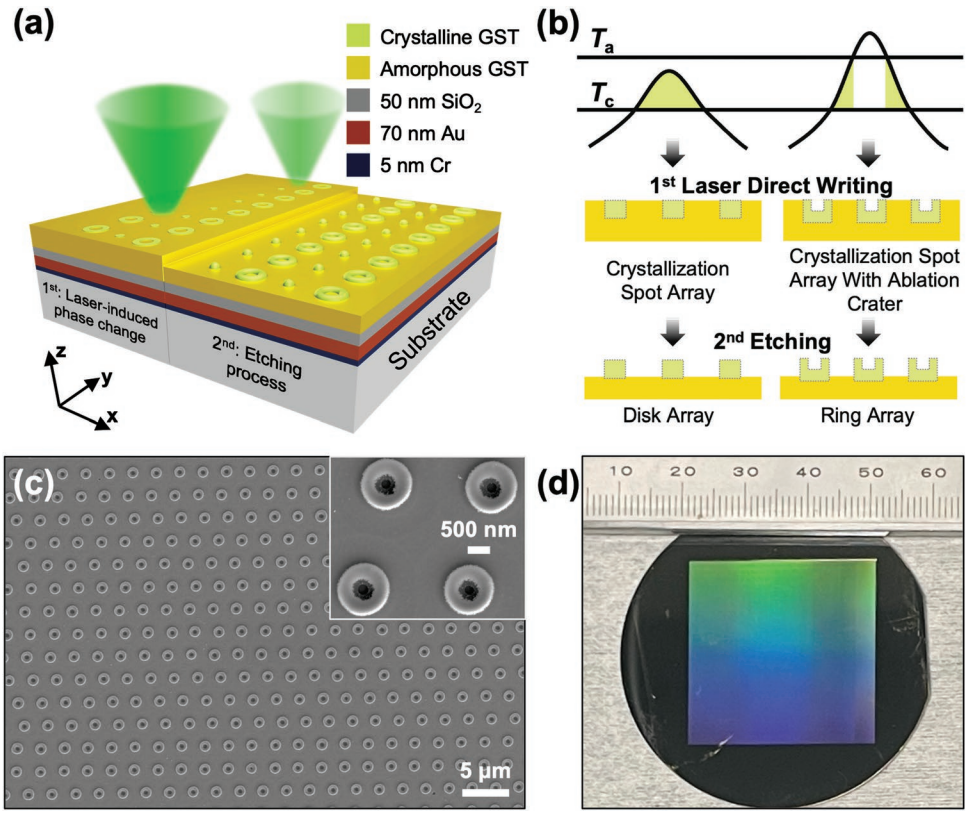


**Figure 1.** a) Schematic of the design and fabrication approach for the metasurface-based absorber. b) Mechanisms of the two-step metasurface fabrication method including laser modification and subsequent etching for achieving different structures. c) SEM image of the typical ring structures corresponding to laser fluence of 799.6 mJ cm$^{-2}$. The scanning speed and scanning interval are 25 mm s$^{-1}$ and 2.5 μm, respectively. d) A highly uniform and large-area ($3 \times 3$ cm$^2$) ring-nanostructured sample. The laser fluence, scanning speed, and scanning interval are 1142.0 mJ cm$^{-2}$, 25 mm s$^{-1}$, and 2.5 μm, respectively. The ring sizes are about 824.0 nm of outer radius, 405.5 nm of inner radius, and 154.8 nm of height. The color variation is due to the optical diffraction.

laser fabrication method. The crystalline GST structure array provides electric and magnetic resonances and the amorphous GST layer can be switched to the crystalline phase acting as a modulation layer. 50-nm thick $SiO_2$ spacer layer and 70-nm thick gold mirror are sandwiched between the GST layer and a fused silica substrate. In addition, a 5-nm thick Cr film is deposited under Au film as the adhesion layer (see the "Experimental Section"). Here, we utilize two processing steps to fabricate structure arrays for our metasurface absorbers. Firstly, the amorphous GST was locally crystallized with or without ablation by tuning laser fluences. Secondly, structures were generated via a subsequent etching process by exploiting the different etching rates of the crystalline and amorphous GSTs.

Figure 1b illustrates the fabrication mechanism of different structures during the two-step fabrication process. When the laser fluence lies between the crystallization threshold ($T_c$) and ablation threshold ($T_a$) of GST, a crystalline spot can be formed on the surface of GST sample. While if the peak fluence is higher than the ablation threshold, an ablation crater smaller than the diffraction limit can be formed with crystallized surroundings. Since the crystalline and amorphous GSTs have different etching rates in alkaline etchant [25 wt% Tetramethylammonium hydroxide (TMAH) solution], disk structure and ring structure can be formed with different laser fluences after etching. Analogous properties are also found in other phase-change materials like silicon.[34] A scanning electron microscope (SEM) image of a typical ring structure is shown in Figure 1c, and fabrication of hybrid structures composed of disks and rings is also depicted in Figure S1 showing the flexibility of this manufacturing method. The period of the depicted units of 2.5 μm depends on the relationship between the laser scanning speed and pulse repetition frequency and it is chosen according to the simulation results in Figure S2. The heights of disk and ring structures can be tuned by controlling etching time and limited by the modification depth and different etching resistance between crystalline and amorphous states of GST. After the etching process, the amorphous GST layer reduces to about 90 nm which is estimated by the etching rate of crystallized GST and the measured height of the structures (see details in Experimental Section). Figure 1d shows an overall morphology of the fabricated sample with a large size (about $3 \times 3$ $cm^2$) demonstrating homogeneity of the sample. The size of fabrication area is also able to scale up to a larger wafer size and does not suffer from the stitching problem which usually appears when preparing large-area subwavelength structures by deep ultraviolet (DUV) photolithography due to the limited exposure area. There are over $10^8$ units in total and the processing speed is 10 000 units per second with a repetition frequency of 10 kHz and a scanning speed of 25 mm $s^{-1}$ in our experiments. The fabrication efficiency only depends on the achievable scanning speed for separate pulse laser irradiation if a high-enough laser repetition frequency is used without considering the acceleration time. Besides disk and ring structures fabricated by the Gaussian beam, it is possible to expand the diversity of the achievable structures through a beam shaping method, whereas, how to achieve the sub-wavelength structural resolution by spatially shaped beams is still an open question.

### 2.2. Effect of Laser Fluence on the Morphology and Size of GST Structures

To investigate the effect of laser fluence on the morphology and size of GST structures, experiments were performed with gradually increased laser fluences with results as shown in **Figure 2**a. Disk structures are formed at lower laser fluences, while ring structures generate at higher laser fluences with ablation in laser spot center. As indicated in Figure 2b, the radiuses (inner radiuses $R_{inner}$ for ring structures) of GST structures are demonstrated as the function of laser fluences, which enables the size of structure to be tunable. The outer radiuses of structures $R_{outer}$ ranging from 251.2 nm to 932.5 nm, and inner radiuses of rings ranging from 284.7 nm to 474.5 nm are available by tailoring the laser fluences. SEM insets of selected typical structures are presented in Figure 2c–i, which clearly show the morphological evolution of the fabricated structures. Figure 2j,k further exhibit the cross-section profiles of typical patterns measured by atomic-force microscope (AFM). A smaller laser fluence corresponding to a lower crystallization degree generally results in a larger etching rate.[35] Thus, the Gaussian beam energy contributes to the parabolic-like cross-sectional profile of the disk structures (Figure 2j) and the sloping outer wall of the M-shaped cross-sectional ring structures (Figure 2k). Vertical sizes of ring structures can be characterized by two physical quantities, which are the height of the outer wall of rings and the depth of the middle position of rings, as indicated in Figure S3. In most cases of fabricated samples, the height and depth of ring are almost equal to each other, see S3 of Supporting Information for a detailed description, so only height of ring is considered in the following discussions. It has to be mentioned that the achievable minimum feature sizes can be further reduced by employing a smaller laser spot through a laser with shorter wavelengths (like DUV laser direct writing) or an objective lens with higher NA.

### 2.3. Spectral Analysis and Absorption Mechanism

The experimental mid-infrared absorptivities of metasurfaces with planar and two different structured surfaces are compared in Figure S4a with their simulation results presented in Figure S4b. The simulation was carried out by FDTD (Finite-difference time-domain) method, in which the relative permittivities of Au, $SiO_2$ and Cr are obtained from Palik,[36] and the relative permittivity of GST refers to the literature[25,37] as listed in the Experimental Section. The disk and ring structures are ideally simplified as a hemi-ellipsoid and a perfect ring in simulations, respectively, whose size parameters are set by referring to the measured morphology. The disk structure is simplified to a hemi-ellipsoid instead of a perfect disk because the hemi-ellipsoid is closer to the measured morphology. The simulated results are in good agreement with the measured results, which verifies the effectiveness of the adopted simulation parameters. Besides, it can be seen that the absorption peak is very low for the unpatterned planar device compared with those structured devices with slightly improved single and largely improved dual absorption peaks corresponding to the disk and ring structures.

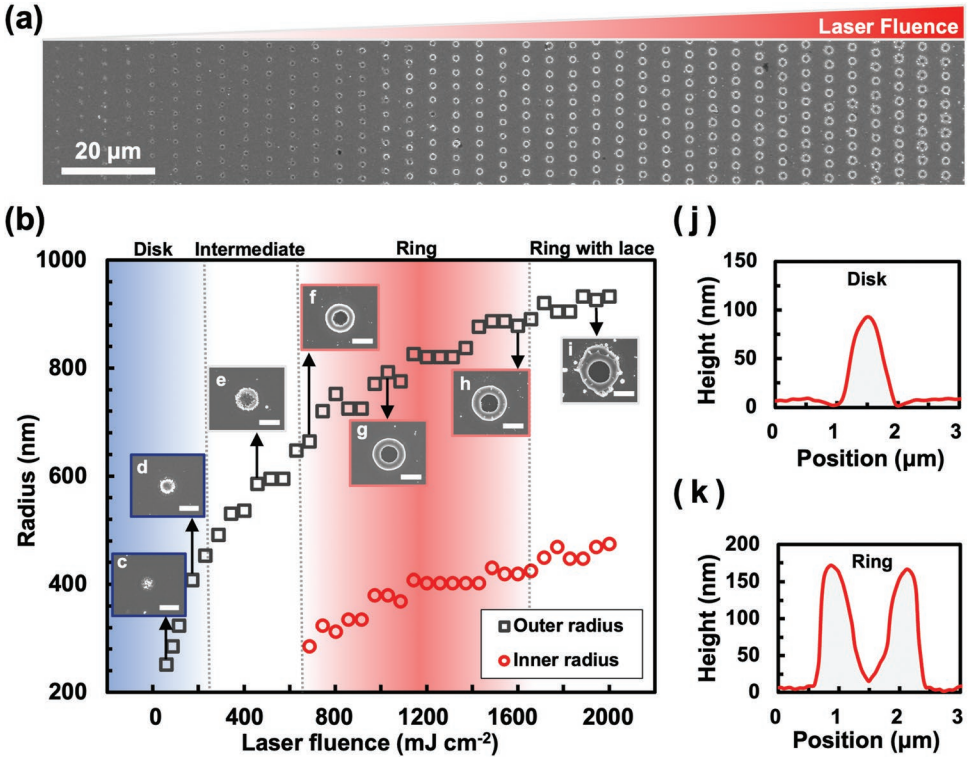


**Figure 2.** Morphological modulation of the GST unit structures by adjusting laser fluences. a) SEM images of a GST sample after laser irradiation with fluences linearly changed from 58.4 mJ cm$^{-2}$ to 1998.8 mJ cm$^{-2}$. b) Effects of laser fluence on the size and morphology of GST structures. The insets (c)–(i) present the morphological evolution of GST nanostructure after laser irradiation of increased fluences and the etching process. Scale bars are 1 μm. j,k) AFM cross-section profiles of the disk and ring structures fabricated at laser fluences of 199.6 mJ cm$^{-2}$ and 1200.5 mJ cm$^{-2}$, respectively.

Thus, we choose ring structure as the unit of the absorber in the following research.

For the ring-type resonators, the absorption peaks can be tuned by changing the sizes of GST patterns. We fabricated a series of ring arrays with laser fluences varying from 970.8 mJ cm$^{-2}$ to 1199.2 mJ cm$^{-2}$. **Figure 3**a shows the experimentally measured absorptivities of the ring-based absorber with different laser fluences. With the increase of laser fluences, the first absorption peak gradually evolves into two peaks, thus the dual-band absorption becomes tri-band absorption, and redshifts of the last absorption peaks are observed in the measured spectra. The corresponding simulated spectra are demonstrated in Figure 3b. According to the results in section 2.2, the outer radius, inner radius, and height of the rings are simultaneously tuned in a certain range by varying the laser fluences. Therefore, we performed simulations with simultaneously changed multiple size parameters (Figure 3b) as well as changing these size parameters individually (Figure S5a–c). We set three groups of multiple size parameters, condition 1 ($R_{outer}$ = 500 nm, $R_{inner}$ = 300 nm, $H$ = 100 nm), condition 2 ($R_{outer}$ = 600 nm, $R_{inner}$ = 350 nm, $H$ = 120 nm), and condition 3 ($R_{outer}$ = 700 nm, $R_{inner}$ = 400 nm, $H$ = 140 nm), respectively. It can be seen in Figure 3b that a redshift of the last absorption peak occurs and a dual-band absorption becomes tri-band with the multiple parameter changes from condition 1 to condition 3, which are consistent with the measured spectra to some extent. The simulations for individual changes in size parameters were performed to provide trends in the effect of individual variables on absorption peaks. In Figure S5a, $R_{outer}$ changes while fixing $R_{inner}$ at 300 nm and $H$ at 130 nm, $R_{inner}$ varies while $R_{outer}$ is fixed at 550 nm and $H$ is 130 nm in Figure S5b, and $H$ changes while setting $R_{outer}$ at 600 nm and $R_{inner}$ at 300 nm in Figure S5c. We show redshift, blueshift, and redshift of the last peak of absorption spectra with the individually increased size parameters of outer radius, inner radius, and height, respectively. The increase in outer diameter promotes less redshift of the last peak compared with the height, but it contributes more to the appearance of the three peaks. The ring-structured absorbers are also insensitive to polarization because the unit of structure arrays is center symmetric, which is proved by the results shown in Figure S6 of the Supporting Information.

To explain the mechanisms of the ring-structure-based absorber, we extracted the electric field distributions within various section planes at the absorption peaks for condition 1 and condition 3 and presented them in **Figure 4** and **Figure 5**, respectively. The typical dual-band and tri-band absorption peaks are marked as $\lambda_{a1}$, $\lambda_{a2}$, $\lambda'_{a1}$, $\lambda'_{a2}$ and $\lambda'_{a3}$ as presented in Figure 3b. It can be seen from the $|E|$ distributions of the $XZ$ plane at $y$ = 0 μm in Figure 4d,i and Figure 5d,i,n that the electric fields mainly concentrate in the $SiO_2$ layer, while they are relatively weak inside the ring structure, and even weaker inside the GST layer. This is because the permittivity (at 35~45 and 15~20) for the crystalline and amorphous GST is much larger than that (~2.13) for the $SiO_2$. As the electric

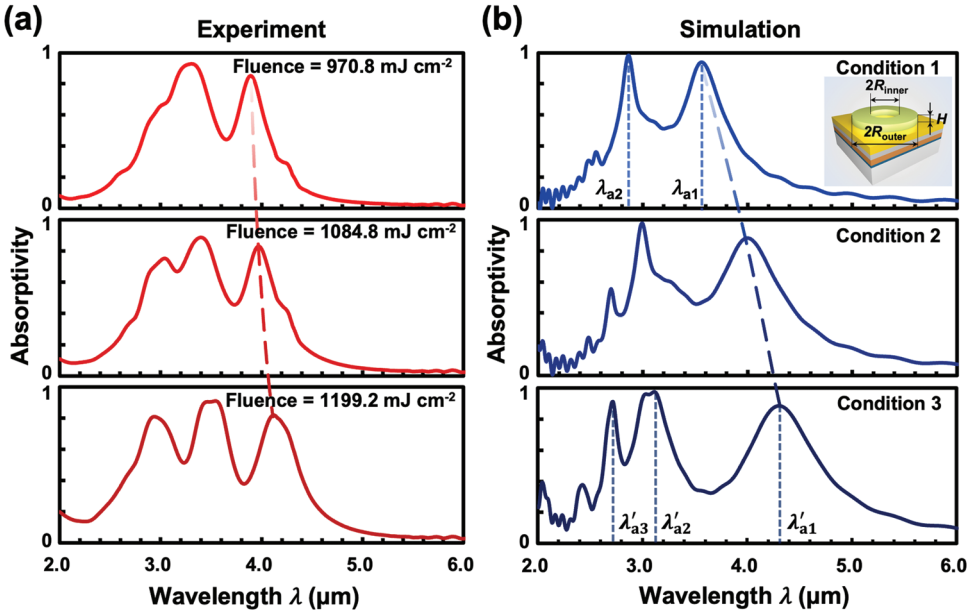


**Figure 3.** a) Measured absorptivities of samples fabricated with varied laser fluences of 970.8 mJ cm$^{-2}$, 1084.8 mJ cm$^{-2}$, and 1199.2 mJ cm$^{-2}$. b) Simulated absorptivities for condition 1 ($R_{outer}$ = 500 nm, $R_{inner}$ = 300 nm, $H$ = 100 nm), condition 2 ($R_{outer}$ = 600 nm, $R_{inner}$ = 350 nm, $H$ = 120 nm), and condition 3 ($R_{outer}$ = 700 nm, $R_{inner}$ = 400 nm, $H$ = 140 nm). The inset shows sketch of the ring unit cell. For the marks of $\lambda_{a1}$, $\lambda_{a2}$, $\lambda'_{a1}$, $\lambda'_{a2}$ and $\lambda'_{a3}$, "a" represents "amorphous GST layer".

displacement perpendicular to the interface is continuous, the electric field inside $SiO_2$ is much larger than that inside the GST layer. As a result, the surface plasmon polaritons (SPPs) excited at the $SiO_2$-Au interface form a standing wave, a mode with electric field distributions quite similar to that observed in metal-dielectric-metal nanocavities in patch antennas.[38]

For the resonant mode at $\lambda_{a1}$ under condition 1, it can be seen that the electrical fields underneath the ring form a magnetic dipole inside the $SiO_2$ layer (Figure 4a,d), similar to the (1,1) mode formed in a circular patch nanoantenna.[39,40] In contrast, an electric quadrupole mode is excited in the ring (Figure 4c,e). For the resonant mode at $\lambda_{a2}$, we can see from the electric fields distribution that the standing waves are formed with similar multiple antinodes inside both the $SiO_2$ layer and the ring structure layer (Figure 4f–h,j), indicating the excitation of a lattice mode. Like the case at $\lambda_{a1}$, the electric fields underneath the ring structure form a magnetic dipole mode inside the $SiO_2$ layer (Figure 4f,i).

When the ring sizes (including the outer radius, inner radius, width of the ring and height) become larger, three absorption peaks appear, namely $\lambda'_{a1}$, $\lambda'_{a2}$ and $\lambda'_{a3}$. For the absorption peak of $\lambda'_{a1}$, the electric field distributions (Figure 5a–e) are the same as those at $\lambda_{a1}$ under condition 1 (Figure 4a–e), indicating the same resonant mode for these two absorption peaks. While for the absorption peak of $\lambda'_{a2}$ (Figure 5f–j), the electric field distributions are quite different from those under condition 1, forming a multipole mode similar to the (1,2) mode in a circular patch nanoantenna,[39,40] Further, we can see antinodes at similar positions in both the $SiO_2$ and the ring structure layers, indicating the excitation of lattice mode. For the third absorption peak of $\lambda'_{a3}$ (Figure 5k–o), it can be seen that a magnetic dipole excited in the $SiO_2$ layer coupled with a lattice mode in both the $SiO_2$ and the ring structure layers.

Given the achievable phase-change property of GST material, we demonstrate the tunable ability of absorption spectra of the designed absorbers after phase transition from amorphous to crystalline of the remained GST layer. Since the phase transition happens when GST is heated above its crystallization temperature of 160 °C, we employ a hotplate to trigger the crystallization transition by heating the sample at 180 °C for 2 minutes.[41] As shown in **Figure 6**a, the absorption peaks undergo pronounced redshifts up to 700 nm after crystallization, while maintaining a high absorption in the mid-infrared region. To investigate the origin of this phenomenon, simulations were performed with amorphous and crystalline states of GST layers. The results agree well with the experimental results as shown in Figure 6. This significant modulation for the absorption wavelength is facilitated by the large difference in the refractive index of amorphous and crystalline GST.[42] The electric field distributions at the two absorption peaks for the crystalline GST layer in Figure 6b are presented in Figure S7. Similar to the case with amorphous GST layer, the electric fields concentrate inside the $SiO_2$ layer at the absorption peaks due to the excitation of surface plasmon waves at the $SiO_2$-Au interface. For the absorption peak of $\lambda_{c1}$ (Figure S7a–e), the electric field distributions are similar to those at absorption peaks of $\lambda_{a1}$ (Figure 4a–e) and $\lambda'_{a1}$ (Figure 5a–e), indicating the same resonant mode for these absorption peaks. While for the second absorption peak of $\lambda_{c2}$, the magnetic dipole mode inside the $SiO_2$ layer (Figure S7f,i) is coupled with a lattice mode in the ring layer, forming two linear antinodes in the $X$ direction (Figure S7g,h,j). This resonant mode is fundamentally different from that for the case of

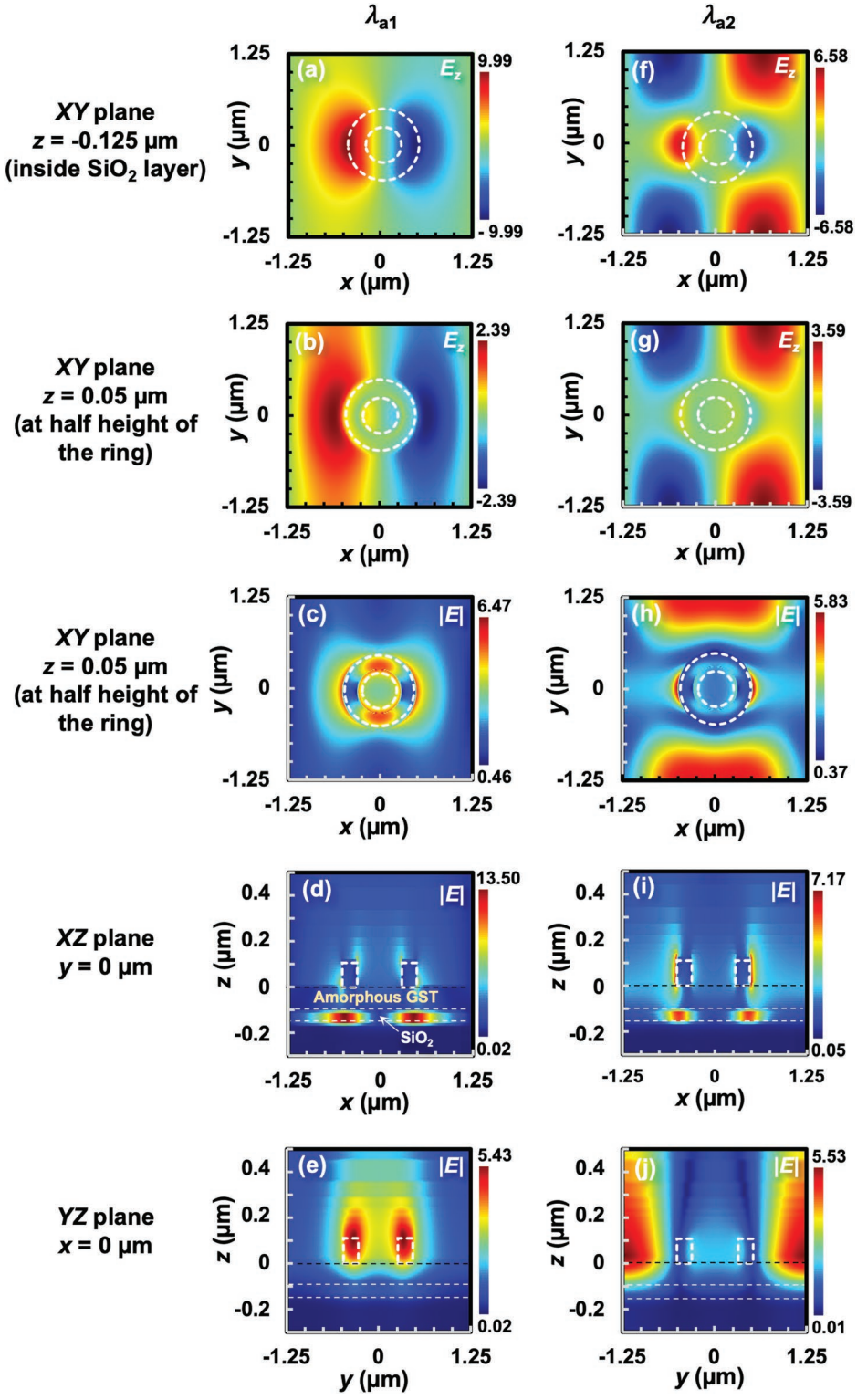


**Figure 4.** Electric field distributions of different planes at absorption peaks of a–e) $\lambda_{a1}$ and f–j) $\lambda_{a2}$ in Figure 3b. (a,f) *XY* plane at $z = -0.125$ μm (inside the $SiO_2$ layer), (b,g,c,h) *XY* plane at $z = 0.05$ μm (at half height of the small ring), (d,i) *XZ* plane at $y = 0$ μm, and (e,j) *YZ* plane at $x = 0$ μm.

the amorphous GST layer ($\lambda_{a2}$). It has to be mentioned that the crystalline GST can possibly switch back to amorphous state by melting and quenching at a cooling rate of $10^9$–$10^{10}$ K $s^{-1}$ which can be achieved by appropriate short-pulse laser or electrical pulses treatments combined with a carefully thermally designed structure.[13,43]

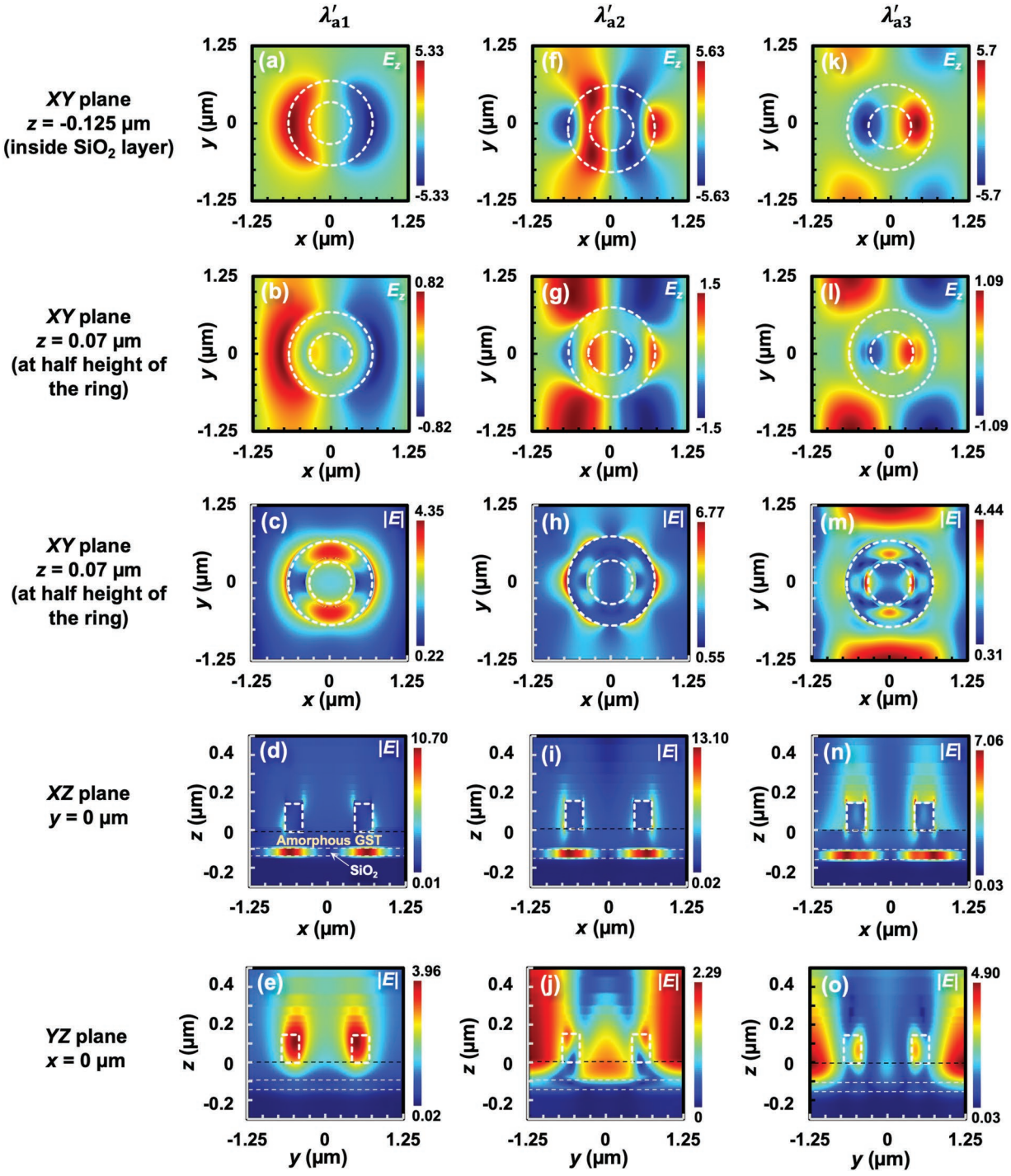


**Figure 5.** Electric field distributions of different planes at absorption peaks of a–e) $\lambda'_{a1}$, f–j) $\lambda'_{a2}$ and k–o) $\lambda'_{a3}$ in Figure 3b. (a,f,k) *XY* plane at $z = -0.125$ μm (inside the $SiO_2$ layer), (b,g,l,c,h,m) *XY* plane at $z = 0.07$ μm (at half height of the large ring), (d,i,n) *XZ* plane at $y = 0$ μm, and (e,j,o) *YZ* plane at $x = 0$ μm.

## 3. Conclusion

We develop a low-cost and high-efficient nanofabrication method by combining separate pulse laser ablation and subsequent etching to fabricate ring structures over a wafer-sized area. The fabrication efficiency linearly depends on the achievable scanning speed for separate pulse laser irradiation under a high-enough laser repetition frequency ensuring the high efficiency. Variation in structure type, size, and period can be achieved simply by adjusting the laser fluence and scanning conditions. By exploiting the achievable nanostructures, a multiband phase-change metasurface absorber with tunable

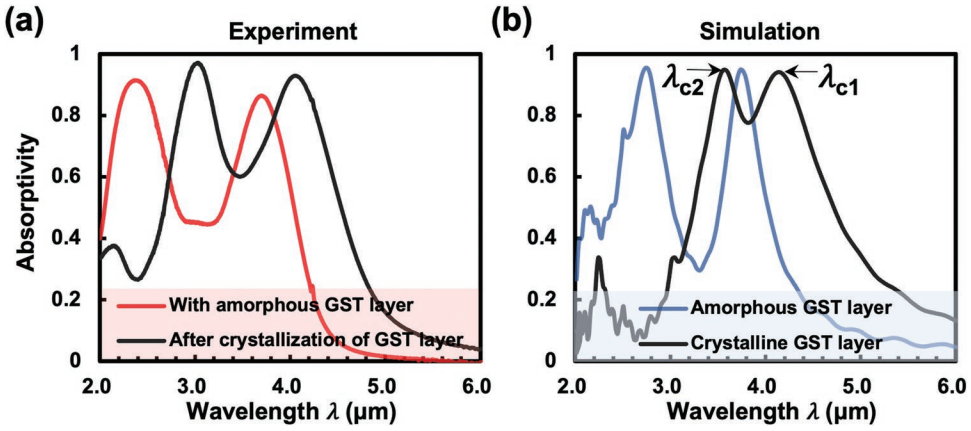


**Figure 6.** a) Experimental and b) simulated results of absorption spectra of the absorber with amorphous GST layer and after crystallization. For the marks of $\lambda_{c1}$ and $\lambda_{c2}$, "c" represents "crystalline GST layer".

bands in the mid-infrared wavelength is designed and manufactured. The absorption peaks can be tuned by varying the sizes of structures, and a shift of the wavelength up to 700 nm can be achieved by the GST phase transition. The designed absorber can be used in applications where multispectral control of mid-infrared signals is required, and the proposed manufacturing method is potential for mass production of the ring-structure-based devices with low cost and high efficiency.

## 4. Experimental Section

*Sample Fabrication*: Fused silica substrates were ultrasonically cleaned with alcohol and isopropanol for 10 min, respectively. Then 5 nm of chromium (Cr) and 70 nm of gold (Au) are evaporated onto the substrate by electron-beam evaporation (HHV, TF500). After that, 50 nm thick $SiO_2$ film and 250 nm of GST film were deposited on top of the Au layer by magnetron sputtering (KYKY, 500CK-500ZF).

For the laser direct writing processes, a femtosecond laser system (Spectra-Physics) provided a Gaussian light spot with a 300 fs pulse width and 520 nm central wavelength. The repetition rate of laser pulses was set to be 10 kHz. The laser beam was focused by a 0.75 NA, 40× objective lens with a beam waist radius of 1.1 μm, and a high-precision moving stage with the step resolution of 10 nm in both *x*- and *y*-axis was employed to control the movement of the sample. The applied laser fluence ranged from 58.4 to 1998.8 mJ $cm^{-2}$ for disk and ring nanostructure fabrication. The scanning speeds and scanning intervals of the experiment were 25 mm $s^{-1}$ and 2.5 μm, respectively, which could also be altered to achieve different pattern periods.

An alkaline etchant [Tetramethylammonium hydroxide (TMAH) solution, 25 wt%] was used to etch the phase-changed GST to obtain disk and ring nanostructures. The etching time is 18 min at room temperature (25 °C) and the etching rate for crystalline and amorphous GST at this condition were about 1.1 and 8.9 nm $min^{-1}$, respectively. The method for measuring the etching rate followed two steps: first, a crystallized GST area with an appropriate scale was fabricated by laser scanning with a certain laser fluence, and then the height difference was measured between the crystalline area and the blank substrate surface after etching by a stylus profilometer (Surfcom NEX 031), then the etching amount of crystallized area for a certain etching time could be obtained and the etching rate can be calculated.

The etched device is further annealed at 180 °C on a hotplate to implement a phase change for tunable absorption.

*Simulation Method*: Finite-difference time-domain simulations (FDTD, Lumerical) were carried out to calculate corresponding optical properties of the structure arrays in the mid-infrared spectral range as well as to reveal the physical absorption mechanism from the electromagnetic field distributions. In the simulation, the relative permittivities of Au, $SiO_2$, and Cr were obtained from Palik.[36] The relative permittivities of amorphous GST and crystalline GST referred to the literature.[25,37] They could also be derived from the literature.[44–47] The periodic boundary conditions were applied in the *x* and *y* directions, and the perfectly matched layer (PML) boundary condition was set along the *z*-direction. The incident light was set to be a plane wave with a band from 2.0 to 6.0 μm. It propagated along the *z*-direction with the polarization being along the *x*-direction.

*Sample Characterization*: Morphology of the structure arrays was measured by scanning electron microscope (SEM, Zeiss, Merlin) and atomic force microscope (AFM, Bruker, Dimension edge). Since the Au film was sufficiently thick, transmission could be neglected, the absorptivity of sample was derived by measuring the reflectivity. The reflectivities of absorber devices were measured by a Fourier transform infrared spectrometer (Bruker, Vertex 70) incorporated with an infrared microscope (Bruker, Hyperion 2000).

## Supporting Information

Supporting Information is available from the Wiley Online Library or from the author.

## Acknowledgements

This work was funded by the Guangdong Provincial University Science and Technology Program (Grant No. 2020KTSCX119) and the Shenzhen Science and Technology Programs (Grant Nos. 20200925155508001, GJHZ20190820151801786, JCYJ20210324115608024, KQTD20170810110250357). Southern University of Science and Technology Core Research Facilities is acknowledged for providing access to all the SEM data and deposition equipment. The authors thank Prof. Guixin Li and Prof. Qihuo Wei at Southern University of Science and Technology for valuable discussions.

## Conflict of Interest

The authors declare no conflict of interest.

## Data Availability Statement

The data that support the findings of this study are available in the supplementary material of this article.

## Keywords

large-scale nanopatterning, metasurfaces, mid-infrared absorption, phase-change materials, separate pulse laser ablation

Received: April 22, 2022
Revised: July 10, 2022
Published online:

[1] N. Yu, P. Genevet, M. A. Kats, F. Aieta, J.-P. Tetienne, F. Capasso, Z. Gaburro, *Science* **2011**, *334*, 333.
[2] M. Diem, T. Koschny, C. M. Soukoulis, *Phys. Rev. B* **2009**, *79*, 033101.
[3] S. Bagheri, N. Strohfeldt, F. Sterl, A. Berrier, A. Tittl, H. Giessen, *ACS Sens.* **2016**, *1*, 1148.
[4] M. A. Butt, S. N. Khonina, N. L. Kazanskiy, R. Piramidowicz, *Opt. Mater.* **2022**, *123*, 111906.
[5] K. Chen, R. Adato, H. Altug, *ACS Nano* **2012**, *6*, 7998.
[6] Y. Zhou, Z. Qin, Z. Liang, D. Meng, H. Xu, D. R. Smith, Y. Liu, *Light: Sci. Appl.* **2021**, *10*, 138.
[7] N. Liu, M. Mesch, T. Weiss, M. Hentschel, H. Giessen, *Nano Lett.* **2010**, *10*, 2342.
[8] Z. Li, L. Stan, D. A. Czaplewski, X. Yang, J. Gao, *Opt. Express* **2018**, *26*, 5616.
[9] Q. He, S. Sun, L. Zhou, *Research* **2019**, *2019*, 1849272.
[10] N. Mou, S. Sun, H. Dong, S. Dong, Q. He, L. Zhou, L. Zhang, *Opt. Express* **2018**, *26*, 11728.
[11] Q. Wang, E. T. F. Rogers, B. Gholipour, C.-M. Wang, G. Yuan, J. Teng, N. I. Zheludev, *Nat. Photonics* **2016**, *10*, 60.
[12] Y. Wang, P. Landreman, D. Schoen, K. Okabe, A. Marshall, U. Celano, H.-S. P. Wong, J. Park, M. L. Brongersma, *Nat. Nanotechnol.* **2021**, *16*, 667.
[13] Y. Zhang, C. Fowler, J. Liang, B. Azhar, M. Y. Shalaginov, S. Deckoff-Jones, S. An, J. B. Chou, C. M. Roberts, V. Liberman, M. Kang, C. Ríos, K. A. Richardson, C. Rivero-Baleine, T. Gu, H. Zhang, J. Hu, *Nat. Nanotechnol.* **2021**, *16*, 661.
[14] Y. G. Chen, T. S. Kao, B. Ng, X. Li, X. G. Luo, B. Luk'yanchuk, S. A. Maier, M. H. Hong, *Opt. Express* **2013**, *21*, 13691.
[15] P. Hosseini, C. D. Wright, H. Bhaskaran, *Nature* **2014**, *511*, 206.
[16] S. Kozyukhin, M. Smayev, V. Sigaev, Y. Vorobyov, Y. Zaytseva, A. Sherchenkov, P. Lazarenko, *Phys. Status Solidi B* **2020**, *257*, 1900617.
[17] C. H. Chu, M. L. Tseng, J. Chen, P. C. Wu, Y. H. Chen, H. C. Wang, T. Y. Chen, W. T. Hsieh, H. J. Wu, G. Sun, D. P. Tsai, *Laser Photonics Rev.* **2016**, *10*, 986.
[18] X. Tian, Z.-Y. Li, *Photonics Res.* **2016**, *4*, 146.
[19] C. Choi, S. Lee, S. Mun, G. Lee, J. Sung, H. Yun, J. Yang, H. Kim, C. Hwang, B. Lee, *Adv. Opt. Mater.* **2019**, *7*, 1900171.
[20] W. Bai, P. Yang, J. Huang, D. Chen, J. Zhang, Z. Zhang, J. Yang, B. Xu, *Sci. Rep.* **2019**, *9*, 5368.
[21] M. Wei, Z. Song, Y. Deng, Y. Liu, Q. Chen, *Mater. Lett.* **2019**, *236*, 350.
[22] X. Tian, J. Xu, K. Xu, X. Ma, X. Duan, P. Yang, P. Ding, Z.-Y. Li, *EPL* **2020**, *128*, 67001.
[23] S. Zhang, K. Zhou, Q. Cheng, L. Lu, B. Li, J. Song, Z. Luo, *Appl. Opt.* **2020**, *59*, 6309.
[24] Y. Qu, L. Cai, H. Luo, J. Lu, M. Qiu, Q. Li, *Opt. Express* **2018**, *26*, 4279.
[25] Y. Qu, Q. Li, K. Du, L. Cai, J. Lu, M. Qiu, *Laser Photonics Rev.* **2017**, *11*, 1700091.
[26] N. Mou, X. Liu, T. Wei, H. Dong, Q. He, L. Zhou, Y. Zhang, L. Zhang, S. Sun, *Nanoscale* **2020**, *12*, 5374.
[27] M. Malinauskas, A. Žukauskas, S. Hasegawa, Y. Hayasaki, V. Mizeikis, R. Buividas, S. Juodkazis, *Light: Sci. Appl.* **2016**, *5*, e16133.
[28] W. Q. Li, F. R. Liu, J. C. Guo, Y. Z. Zhang, Y. H. Wang, F. Liu, N. X. Sun, W. Xiao, *Opt. Laser Technol.* **2019**, *111*, 585.
[29] A. Dun, J. Wei, F. Gan, *Chin. Opt. Lett.* **2011**, *9*, 082101.
[30] C. Deng, Y. Geng, Y. Wu, *Appl. Phys. A* **2011**, *104*, 1091.
[31] C. Deng, Y. Geng, Y. Wu, Y. Wang, J. Wei, *Microelectron. Eng.* **2013**, *103*, 7.
[32] K. Zhang, Z. Wang, G. Chen, J. Zheng, Z. Mo, Y. Wang, J. Wei, *Mater. Sci. Semicond. Process.* **2021**, *134*, 106018.
[33] G. Chen, J. Zheng, Z. Wang, K. Zhang, Z. Mo, X. Liu, T. Gao, Y. Wang, J. Wei, *J. Alloys Compd.* **2021**, *867*, 158988.
[34] X. Li, Q. Xie, L. Jiang, W. Han, Q. Wang, A. Wang, J. Hu, Y. Lu, *Appl. Phys. Lett.* **2017**, *110*, 181907.
[35] X. Sun, M. Ehrhardt, A. Lotnyk, P. Lorenz, E. Thelander, J. W. Gerlach, T. Smausz, U. Decker, B. Rauschenbach, *Sci. Rep.* **2016**, *6*, 28246.
[36] E. Palik, *Handbook of Optical Constants of Solids*, Elsevier, San Diego **1998**.
[37] K. Du, Q. Li, Y. Lyu, J. Ding, Y. Lu, Z. Cheng, M. Qiu, *Light: Sci. Appl.* **2017**, *6*, e16194.
[38] B. Joshi, A. Chakrabarty, Q. H. Wei, *IEEE Trans. Nanotechnol.* **2010**, *9*, 701.
[39] F. Minkowski, F. Wang, A. Chakrabarty, Q. H. Wei, *Appl. Phys. Lett.* **2014**, *104*, 10.
[40] A. Chakrabarty, F. Wang, F. Minkowski, K. Sun, Q.-H. Wei, *Opt. Express* **2012**, *20*, 11615.
[41] X. Yin, T. Steinle, L. Huang, T. Taubner, M. Wuttig, T. Zentgraf, H. Giessen, *Light: Sci. Appl.* **2017**, *6*, e17016.
[42] A.-K. U. Michel, M. Wuttig, T. Taubner, *Adv. Opt. Mater.* **2017**, *5*, 1700261.
[43] K. Liu, M. Lian, K. Qin, S. Zhang, T. Cao, *Light: Adv. Manuf.* **2021**, *2*, 251.
[44] D.-X. Zhu, W.-D. Shen, H.-Y. Zhen, *J. Appl. Phys.* **2009**, *106*, 084504.
[45] J. Orava, T. Wágner, J. Šik, J. Přikryl, M. Frumar, L. Beneš, *J. Appl. Phys.* **2008**, *104*, 043523.
[46] G. E. Jellison, F. A. Modine, *Appl. Phys. Lett.* **1996**, *69*, 371.
[47] Z. Xu, C. Chen, Z. Wang, K. Wu, H. Chong, H. Ye, *RSC Adv.* **2018**, *8*, 21040.